Preparation of $0.4Li_2MnO_3 \cdot 0.6LiNi_{1/3}Co_{1/3}Mn_{1/3}O_2$ with tunable morphologies via polyacrylonitrile as a template and applications in lithium-ion batteries

Xiaowei Miao,[1,2] Huan Ni,[1] Xuerong Sha,[1] Ting Wang,[1] Jianhui Fang,[2] Gang Yang[1]

[1]Jiangsu Laboratory of Advanced Functional Materials, Changshu Institute of Technology, Changshu 215500, China
[2]Department of Chemistry, Shanghai University, Shanghai 200444, China
Correspondence to: G. Yang (E-mail: gyang@cslg.edu.cn)

ABSTRACT: Samples of $0.4Li_2MnO_3 \cdot 0.6LiNi_{1/3}Co_{1/3}Mn_{1/3}O_2$ (LMO) with tunable morphologies were synthesized via polyacrylonitrile (PAN) as a template. The starting PAN/N,N-dimethylformamide (DMF) ratios, including 1:9, 1:10, 1:12, and 1:14, were optimized for the fiber morphologies and electrochemical performance. Through electrospinning, metal salts were well dispersed in the PAN fibers. The crystal structure and morphologies of the PAN/LMO fibers were characterized by X-ray diffraction, scanning electron microscopy, and thermal analysis. Along with the decrease in the concentration of PAN in the precursor, the diameters of the PAN/LMO fibers decreased. On the other hand, at the highest and lowest concentrations, 1:9 and 1:14, of PAN with DMF, micrometer PAN fibers were electrospun, whereas ratios of PAN to DMF of 1:10 and 1:12 resulted in the electrospinning of millimeter-long fibers of PAN. In the interface of PAN and metal salts, LMOs were grown and accompanied the decomposition of PAN, and the crystal morphologies of LMO quite depended on the diameter and length of the PAN/LMO nanofibers. During heat treatment, the morphologies of the PAN fibers controlled the removal of small molecules and the crystal morphologies of LMOs. The charge/discharge results indicate that LMO with a tubular structure delivered a capacity of 262.3 mAh/g at a cutoff voltage of 2.5–4.8 V at a 0.1 C rate. Benefitting from a unique hollow and nanocrystalline architecture, it also exhibited good rate and cycling performances. © 2015 Wiley Periodicals, Inc. J. Appl. Polym. Sci. **2016**, *133*, 43022.

INTRODUCTION

In recent years, rechargeable lithium-ion batteries (LIBs) have played a leading role as energy-storage devices for electric vehicles, hybrid electric vehicles, and so on.[1,2] Breakthroughs for high-performance LIBs include improvements in the electrochemical performance in terms of durability, power density, conversion efficiency, cost, and environmental friendliness for large-scaled applications in electric vehicles, hybrid electric vehicles, and so on.[3] Cathode materials play a key role in high-performance LIBs, but the specific capacities of several kinds of commercial cathodes are low. For example, $LiCoO_2$ only delivers 150 mAh/g, the specific capacity of spinel $LiMn_2O_4$ is 120 mAh/g, and that of olivine $LiFePO_4$ is 170 mAh/g.[4]

Mn-based layered compounds written as $Li_{1+x}[M]_{1-x}O_2$ or $xLi_2MnO_3 \cdot (1 - x)LiMO_2$ (where M is Ni, Co, or Mn; $x > 0$)[5,6] are attractive because of high specific capacities of over 250 mAh/g and the safety at a high cutoff voltage of 4.8 V.[7] The structure of these compounds have additional lithium existed in

the transition-metal layer, that called lithium-excess layered oxide compound, compared with conventional structure of $LiCoO_2$.[8] There are several shortcomings in application of the lithium-excess compounds as cathode for LIBs; for instance, a huge irreversible capacity loss presented in the initial charge/discharge cycle, severe capacity fading, and poor rate capability.[6–10] In recent years, many significant efforts have been devoted to reducing the initial irreversible capacity with ionic substitutions, surface modifications, preconditioning with acidic solutions, and so on.[10,11] For example, Jiang et al.[12] reported the preparation of graphene-wrapped lithium-excess layered hybrid materials ($Li_2MnO_3 \cdot LiMO_2$, M = Mn, Ni, and Co), in which the graphene conducting framework efficiently alleviated the polarization of pristine materials; this led to an outstanding enhancement in cell performance and cycling stability. Previous publications have found that the electrochemical properties, for example, the sample in nanosize, of lithium-excess compounds are always influenced by the crystal morphologies.[13–19] To obtain nanosized lithium-excess compounds, there were several

previous studies that focused on synthesis techniques,[17–19] such as sol–gel, coprecipitation, solvothermal treatment, electrospinning, and heat-treatment techniques.

Electrospinning, a simple and cost-efficient method in making nanofibers, has been widely used in the preparation of many one-dimensional compounds as electrode materials for LIBs,[20–30] such as $LiCoO_2$, $Li_2Mn_2O_4$, $LiMnO_2$, $LiNi_{1/3}Co_{1/3}Mn_{1/3}O_2$, and $LiFePO_4$. $LiCoO_2$ and $LiNi_{1/3}Co_{1/3}Mn_{1/3-x}Al_xO_2$ $(0 \leq x \leq 0.08)$ nanofibers reported by Gu et al.[27] and Ding et al.,[28] respectively, were synthesized by electrospinning. The electrospun $LiMnO_2$ nanofibers reported by Sun et al.[24] delivered a reversible discharge capacity of 160 mAh/g. Xu et al.[31] synthesized $0.6Li[Li_{1/3}Mn_{2/3}]O_2 \cdot 0.4Li[Ni_{1/3}Co_{1/3}Mn_{1/3}]O_2$ with different morphologies by electrospinning and a coprecipitation method, respectively. The advantage of electrospinning is that metal salts can be homogeneously dispersed in the polymer matrix, where the polymer is an important template. In the following heat treatment, inorganic compounds with special crystal morphologies were produced, along with the carbonization or oxidation of the polymer. The previous publications mainly focused on the preparation and improvement of the electrochemical performance. Until now, there has been a lack of reports on the morphologies of products controlled by the concentration of the polymer. In particular, the behavior of the removal of polyacrylonitrile (PAN) and the growth of inorganic compounds are unknown. It is urgent to study the preparation and growth mechanism of $xLi_2MnO_3 \cdot (1 - x)LiMO_2$ via PAN fibers as a template.

In this study, $0.4Li_2MnO_3 \cdot 0.6LiNi_{1/3}Co_{1/3}Mn_{1/3}O_2$ (LMO) samples with various crystal morphologies were synthesized via electrospinning and heat treatment. The concentration of PAN in the starting solution PAN/N,N-dimethylformamide (DMF) played an important role in the tunable crystal morphologies of LMOs. In the interface of PAN and metal salts, LMOs were grown; this was accompanied by the decomposition of PAN. The crystal structure, morphology, and decomposition of the PAN/LMO fibers were characterized by X-ray diffraction, scanning electron microscopy (SEM), and thermal analysis. The electrochemical properties of the as-synthesized LMOs were studied in detail.

EXPERIMENTAL

An amount of 4.0 g of PAN (weight-average molecular weight = 150,000, Aldrich) was dissolved in DMF (99.8%, Aldrich) at 80°C with vigorous stirring for 3 h. Amounts of 2.0 g of $Li(CH_3COO)$, $Ni(CH_3COO)_2 \cdot 4H_2O$, $Co(CH_3COO)_2 \cdot 4H_2O$, and $Mn(CH_3COO)_2 \cdot 4H_2O$ in stoichiometric ratios were dissolved in the solution of PAN/DMF. The weight ratios of PAN with DMF were 1:9, 1:10, 1:12, and 1:14. The operating conditions during the fiber production included a flow rate of 5 mL/h, and a distance of 20 cm between the tip and collector was used. Under a voltage of 18 kV, a white film was electrospun and collected from a collector of aluminum foil. The precursor films of metal salts dispersed in PAN were named simply PAN/LMO-A, PAN/LMO-B, PAN/LMO-C, and PAN/LMO-D according to the starting ratios 1:9, 1:10, 1:12, and 1:14, respectively, of PAN/DMF. The white films were

heated at a temperature of 800°C for 3 h under an air atmosphere. LMO samples were synthesized and named simply LMO-A, LMO-B, LMO-C, and LMO-D according to the precursors of PAN/LMO-A, PAN/LMO-B, PAN/LMO-C, and PAN/LMO-D, respectively.

With a Rigaku diffractometer (Dmax-2200) with Cu Kα radiation, the X-ray diffraction patterns were recorded at a scan rate of 2°/min from 10 to 90°. The crystal morphologies were characterized with a scanning electron microscope (Hitachi-X650 microscope, 20 kV) coupled with an energy-dispersive spectroscopy X-ray detector. The thermal decomposition of PAN and LMO crystal growth in PAN/LMO was examined by thermogravimetric analysis (TGA) under an air atmosphere and nitrogen atmosphere, respectively. TGA and differential scanning calorimetry (DSC) of the samples were recorded with a thermogravimetry (TG)–DSC thermal analyzer system (STA449F3, Netzsch).

The electrochemical performances of the samples were collected in CR2016 coin cells. The electrodes of the active materials (80 wt %), Super P (10 wt %), and poly(vinylidene fluoride) (10 wt %) were mixed in N-methyl-2-pyrrolidone and stirred for 1 h. The slurry was cast onto aluminum foil and dried at 120°C for 12 h in vacuo. The loading density of the electrode was about 4 mg/cm^2. The cells were assembled in an argon-filled glovebox with lithium metal as the counter electrode, Celgard 2500 as the separator, and $1M$ $LiPF_6$ dissolved in ethylene carbonate, dimethyl carbonate, and ethyl methyl carbonate with a volume ratio of 1:1:1 as the electrolyte. The galvanostatic charge and discharge tests were made within the voltage range 2.5–4.8 V versus Li^+/Li with a LAND CT2001A battery testing system.

RESULTS AND DISCUSSION

Because the morphologies of the PAN/LMO films were sensitive to the electrospinning parameters, the applied voltage, solution feed rate, and spinning distance, the environmental parameters (e.g., temperature, humidity, air velocity in the chamber) were fixed at the same values, except the starting ratio of PAN with DMF. The concentration of metal salt and PAN in DMF were the main factors in the dispersion of metal salts and fiber morphologies through electrospinning. Figure 1 shows the SEM images of the PAN/LMO fibers. Along with the decrease in the PAN concentration in the precursor, the diameters of the PAN/LMO fibers decreased. The fiber diameters of PAN/LMO-A, PAN/LMO-B, PAN/LMO-C, and PAN/LMO-D were about 2.3, 1.9, 1.4, and 1.0 μm, respectively. On the other hand, PAN/LMO-A electrospun from the highest ratio of PAN with DMF and PAN/LMO-D from the lowest ratio of PAN with DMF presented broken and short fibers, 2.3 μm (diameter) $\times$ 16 μm (length) in PAN/LMO-A and 1.0 μm (diameter) $\times$ 15 μm (length) in PAN/LMO-D. PAN/LMO-B and PAN/LMO-C presented homogeneous and ultralong fibers. The length of the PAN/LMO-B and PAN/LMO-C fibers reached the size of millimeters [as shown in Figure 1(b,c)].

To study the dispersion of metal elements in the PAN matrix, the elemental mappings of PAN/LMO-B were recorded by energy-dispersive spectroscopy analysis and are shown in Figure 2 (other samples are not shown here). The main component
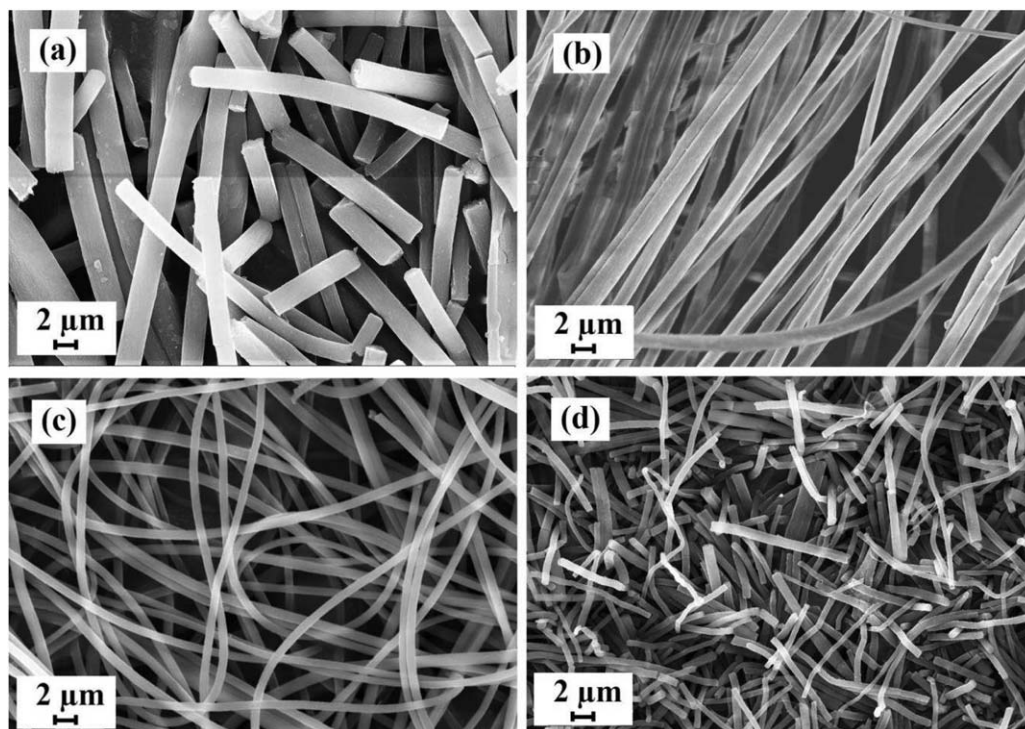
Figure 1. SEM images of (a) PAN/LMO-A, (b) PAN/LMO-B, (c) PAN/LMO-C, and (d) PAN/LMO-D.

was carbon, which came from PAN as a skeleton of fibers [Figure 2(b)]. As shown in Figure 2(c–e), metal elements of Mn, Co, and Ni were well dispersed in the PAN fibers. In the following high-temperature heat treatment, the inorganic compounds of LMOs grew *in situ;* this was accompanied by the removal of organic species where PAN was the template.

Figure 3 shows the Differential Thermal Analysis (TG/DTA) of the PAN/LMOs measured under an air atmosphere. The four samples presented much different TG/DTA curves, although the theoretical weight ratios of PAN and the metal salts were the same. The weight losses of PAN/LMOs under an air atmosphere mainly came from the decomposition of metal salts and the
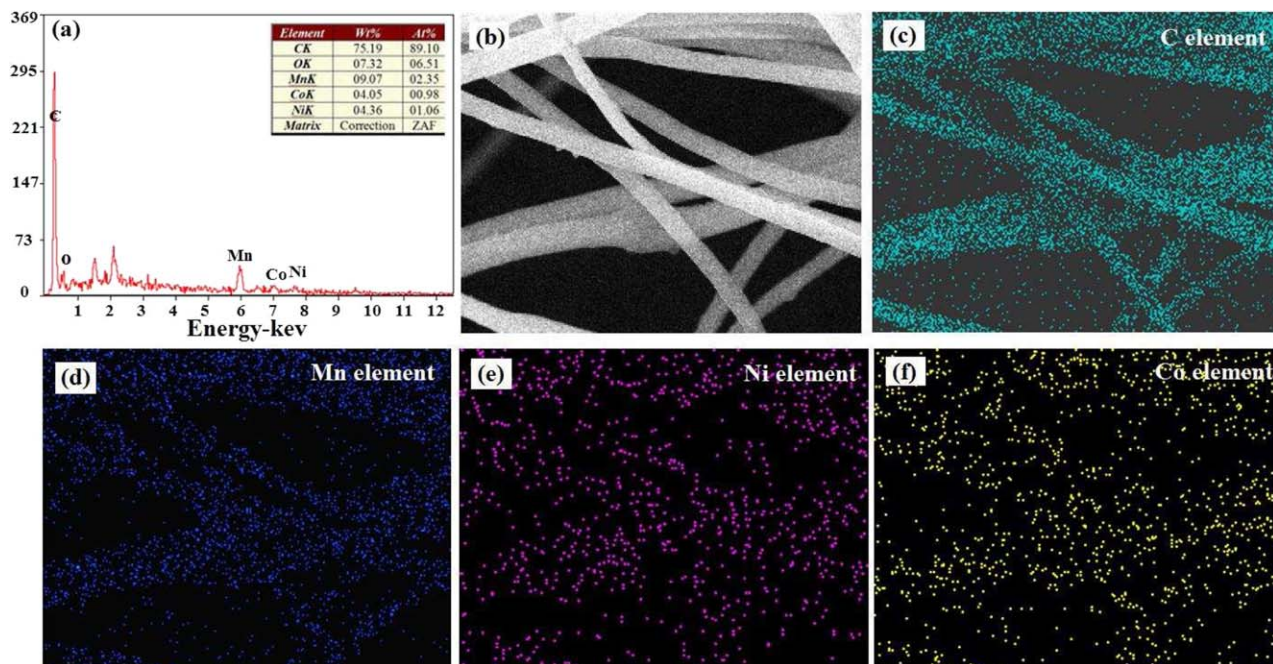

Figure 2. (a) Energy-dispersive spectrum, (b) SEM image, and (c–f) elemental mapping of C, Mn, Ni, and Co for PAN/LMO-B. The atomic compositions in Fig. 2a are calculated by using ZAF method. ZAF: correction factors. [Color figure can be viewed in the online issue, which is available at wileyonlinelibrary.com.]
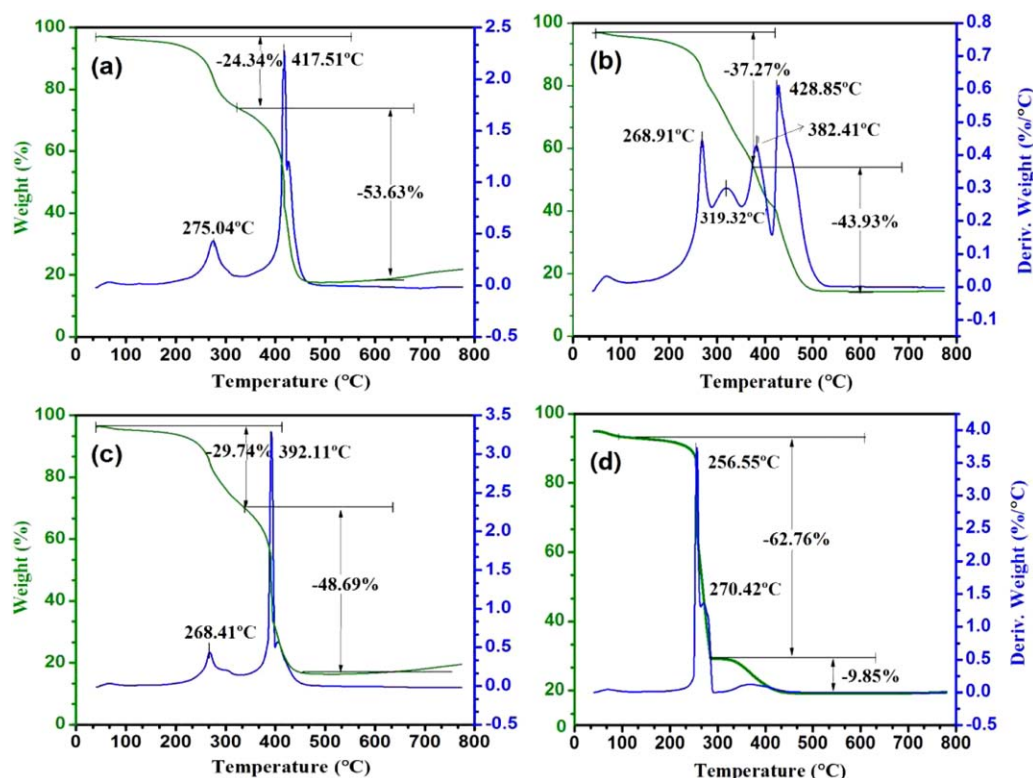
Figure 3. TG/DTA profiles of (a) PAN/LMO-A, (b) PAN/LMO-B, (c) PAN/LMO-C, and (d) PAN/LMO-D under an air atmosphere. [Color figure can be viewed in the online issue, which is available at wileyonlinelibrary.com.]

oxidation of PAN. The crystallization extent of PAN, diameter and length of the fiber, and dispersion of metal salts determined the TG/DTA curves. PAN/LMO-A showed two main weight losses, 24.3% at 200–300°C and 53.6% at 300–420°C; the former mainly came from the decomposition of acetate radicals of the metal salts, and the latter mainly came from the oxidation of PAN. PAN/LMO-D presented main removals of 62.7% around 250°C and 9.85% at 300–400°C because the narrowest fibers of PAN/LMO-D might have been easily decomposed at relatively lower temperatures. PAN/LMO-B presented a continuous weigh loss in the temperature range 250–450°C because of the homogeneous structure of metal salt dispersed in the PAN nanofibers. There might have been a relatively poor connection between the metal salts and PAN macromolecules in PAN/LMO-A and PAN/LMO-C with respect to the two independent weight losses. The proper interaction and distribution of metal salts in PAN/LMO-B were helpful for maintaining the fiber structure of PAN under high-temperature treatment. From the DTA curves, the exothermic peak further reflected the oxidation degree of PAN in the four samples. The main exothermic peaks of PAN/LMO-A, PAN/LMO-B, PAN/LMO-C, and PAN/LMO-D appeared at 417.5, 428.8, 392.1, and 270.4°C, respectively. The smaller diameter of the PAN/LMO nanofiber was, the easier decomposition of PAN was.

TGA/DSC profiles of the PAN/LMO films measured under an N_2 atmosphere showed other kinds of weight losses, as shown in Figure 4; these include the heat degradation of PAN and the growth of LMO crystals. All four samples presented minor

weight losses below 150°C; these were associated with the release of the remaining solvents.[32] Around 264°C, there was a strong exothermic peak corresponding to the physical and chemical changes in PAN; this included exothermic chemical reactions, cyclization, dehydration, oxidation, and crosslinking among PAN chains.[33–35] The weight losses of the four samples appeared around a temperature of 264°C and were attributed to the cyclization of PAN accompanying the removal of small molecules. From 300 to 400°C, the weight losses of PAN/LMO-A, PAN/LMO-B, PAN/LMO-C, and PAN/LMO-D reached 44.7, 42.4, 32.7, and 34.7%, respectively; these were attributed to the degradation and partial removal of PAN. Between 400 and 700°C, the weight loss (ca. 10%) was attributed to the further degradation of the skeleton of the PAN fiber. Beyond 700°C, an inorganic compound of LMO grew; this corresponded to a small exothermic peak at about 750°C and a minor weight loss.

Under high-temperature heat treatment at 800°C for 3 h, two processes simultaneously happened in the PAN/LMO film. One was the oxidation of PAN, and the other was the crystal growth of LMO. Figure 5 shows the X-ray diffraction patterns of LMO-A, LMO-B, LMO-C, and LMO-D. No impurities were observed. The four products presented the same patterns in previous studies.[13–16] The patterns were well indexed to the α-NaFeO$_2$ structure (space group: $R\text{-}3m$) characterized by LiMO$_2$ (M = Ni, Co, Mn, etc.). The weak peaks at $2\theta = 20\text{–}25°$ indexed to monoclinic Li$_2$MnO$_3$ phase ($C\,2/m$) were generally attributed to the ordering of Li$^+$ ions in the transition-metal layer.[36] In general, a higher value (>1.2) of $I_{(003)}/I_{(104)}$, the intensity ratio of the
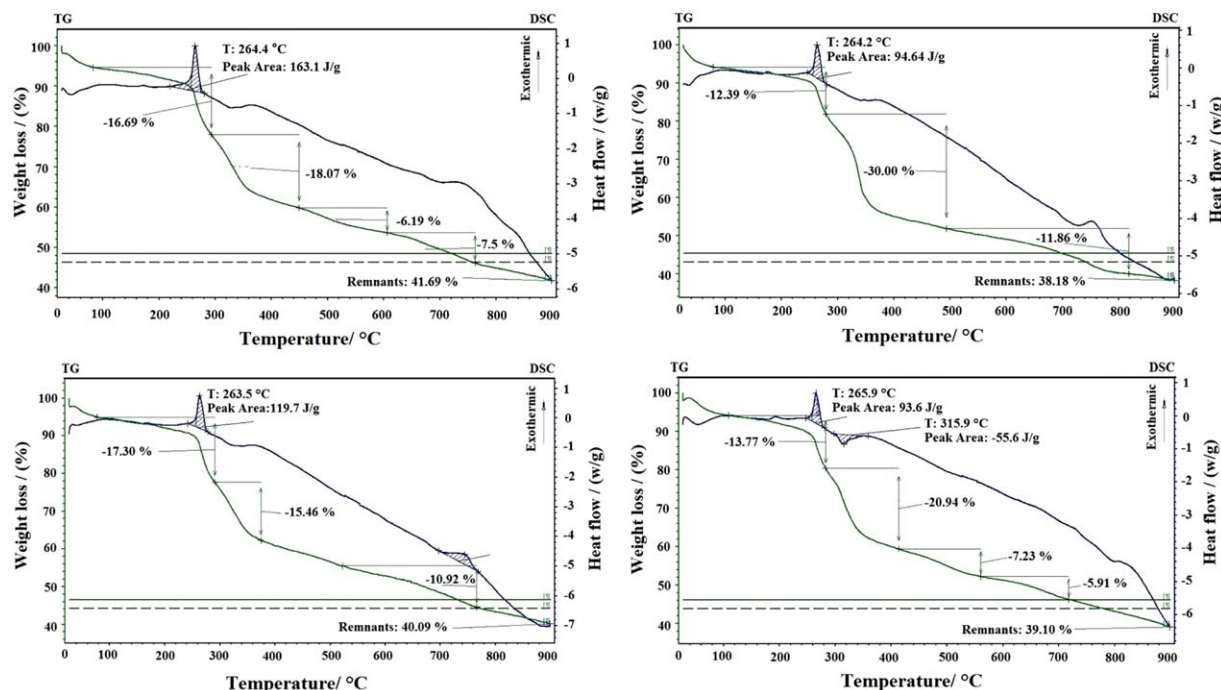
Figure 4. TGA and DSC analysis of (a) PAN/LMO-A, (b) PAN/LMO-B, (c) PAN/LMO-C, and (d) PAN/LMO-D under a nitrogen atmosphere. [Color figure can be viewed in the online issue, which is available at wileyonlinelibrary.com.]

indexed XRD peaks of (003) to (104), is an indicator of lower cation mixing among Li^+, Ni^{2+}, Co^{3+}, and Mn^{4+} cations.[37] In this study, the $I_{(003)}/I_{(104)}$ intensity ratios were 1.36, 1.35, 1.23, and 1.18 in LMO-A, LMO-B, LMO-C, and LMO-D, respectively.

Figure 6 shows the SEM images of LMO products. PAN/LMO-A and PAN/LMO-D were converted to the relatively short cluster [LMO-A in Figure 6(a,a′)] and curved sheet [LMO-D in Figure 6(d,d′)] composed of nanoparticles. The primary nanocrystal sizes of LMO-A and LMO-D were 160 and 100 nm, respectively. PAN/LMO-B and PAN/LMO-C were converted to

Figure 5. X-ray diffraction patterns of (a) LMO-A, (b) LMO-B, (c) LMO-C, and (d) LMO-D. [Color figure can be viewed in the online issue, which is available at wileyonlinelibrary.com.]

long and winding nanofibers of LMO-B and LMO-C, as shown in Figure 6(b,b′,c,c′). The primary nanocrystal sizes of LMO-B and LMO-C were 100 and 70 nm, respectively. LMO-B presented a tubular structure in which the outer diameter was 700–900 nm and the thickness of the wall was estimated to be 100 nm.

To better show the morphological change of the PAN/LMOs during heat treatment, Figure 7 shows the schematic degradation behavior of PAN and the growth behavior of LMO nanoparticles. It shows the schematic steps of metal salt dissolution in the PAN/DMF solution (I), the fibers of PAN/LMO formation via electrospinning (II), and the final product of LMOs growth via the template of PAN fibers (III). Via electrospinning, metal salts were well dispersed in the PAN fibers.[38] At the highest and lowest concentrations, 1:9 and 1:14 of PAN with DMF, short PAN fibers were electrospun in PAN/LMO-A and PAN/LMO-D, whereas ratios of PAN to DMF of 1:10 and 1:12 resulted in the electrospinning of very long fibers of PAN/LMO [as shown in Figure 7(I)]. Under high-temperature heat-treatment, PAN chains were decomposed to small molecules, such as CO_2 and NO_x, and LMO nanoparticles were grown, but the crystal morphologies of LMO quite depended on the diameters and length of the PAN/LMO fibers [as shown in Figure 7(III)]. We propose that the short fibers of PAN were decomposed, and the organic species were removed through the interspace in PAN/LMO; LMO crystals grew and aggregated on the basis of the morphologies of their precursors [Figure 7(a,d)]. On the contrary, the long PAN fibers hindered the removal of small molecules, and the appeared inner pressure resulted in the crystals growing toward the outer fibers to form the tubular structure of LMOs [as shown in Figure 7(b,c)].
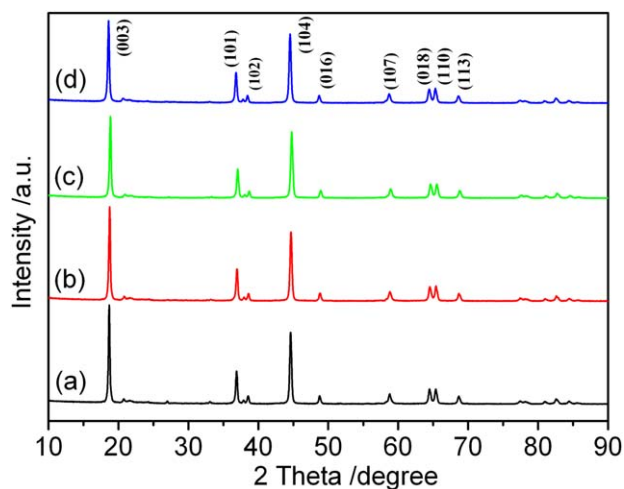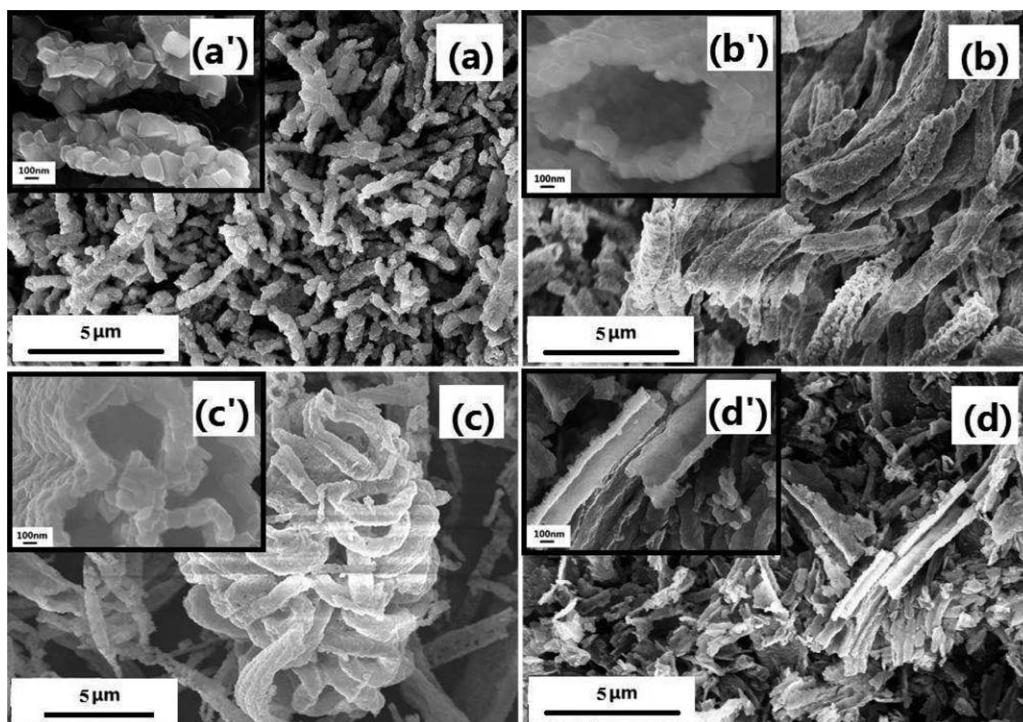
Figure 6. SEM images of (a) LMO-A, (b) LMO-B, (c) LMO-C, and (d) LMO-D.
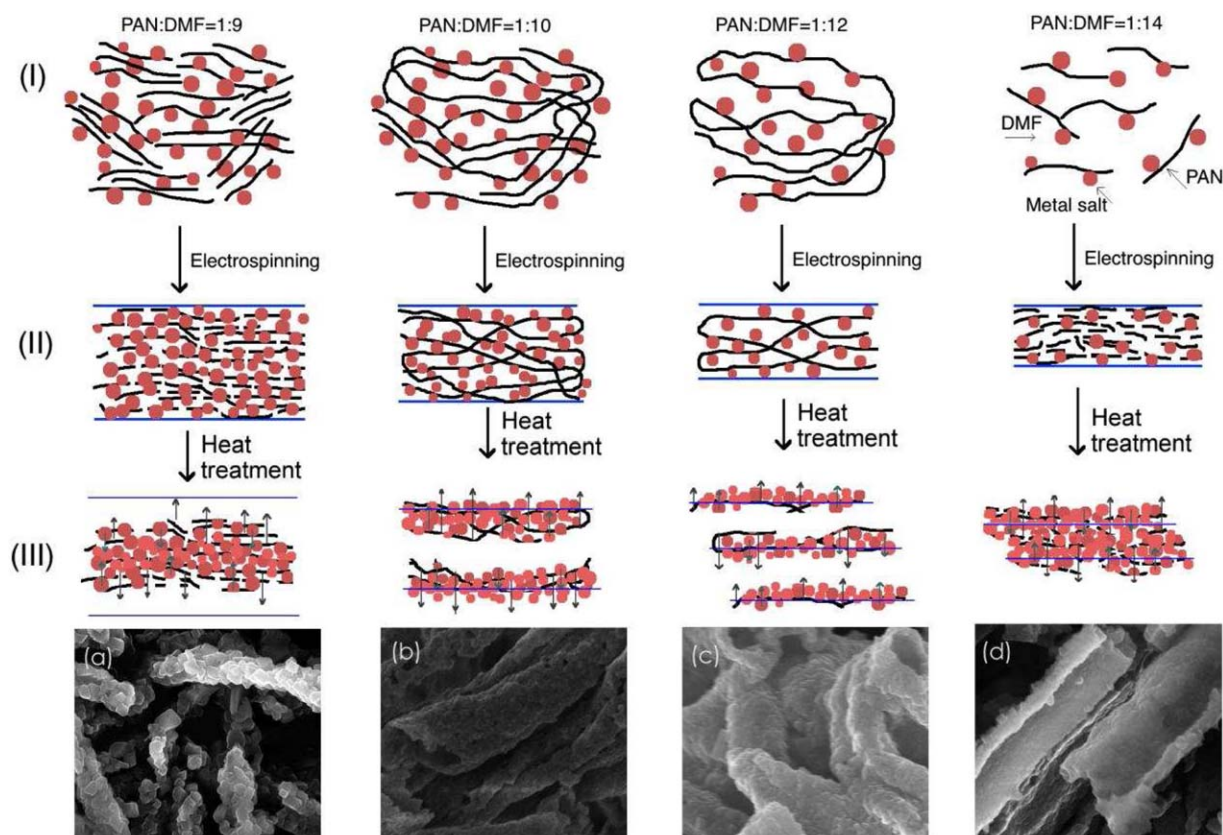

Figure 7. Schemes of (I) metal salt dissolution in a PAN/DMF solution, (II) fibers of PAN/LMO via electrospinning, and (III) final products of (a) LMO-A, (b) LMO-B, (c) LMO-C, and (d) LMO-D via heat treatment. [Color figure can be viewed in the online issue, which is available at wileyonlineli-brary.com.]
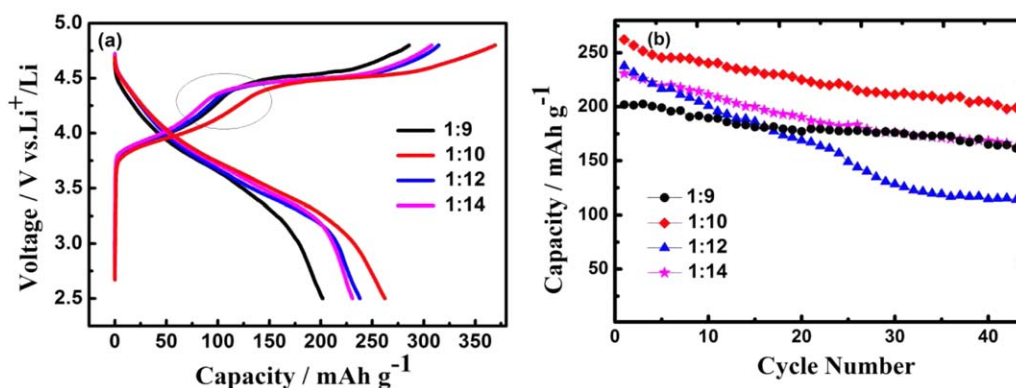
Figure 8. (a) Initial charge/discharge profiles and (b) cycling performance of LMO samples recorded in the voltage range 2.5–4.8 V and at a rate of 0.1 C. [Color figure can be viewed in the online issue, which is available at wileyonlinelibrary.com.]

The crystal morphologies of LMOs also played an important role in the electrochemical performance. Figure 8 presents the initial charge/discharge profiles and cycling performance of the LMO samples. The initial charge profiles included two parts. The part at 3.5–4.5 V was attributed to the oxidation processes of N_i^{2+} to N_i^{4+} and Co^{3+} to Co^{4+}.[39] The voltage plateau beyond 4.5 V was assigned to an irreversible loss of oxygen ($2Li^+ + O^{2-} = Li_2O$) from the structural lattice of the Li_2MnO_3 component.[40] Figure 8(a) shows the initial discharge capacities of 201.9, 262.3, 237.9, and 230.8 mAh/g in LMO-A, LMO-B, LMO-C, and LMO-D, respectively. The LMO-B and LMO-C with a tubular structure delivered better specific capacities than LMO-A and LMO-D. For the initial charge curves [the circle noted in Figure 8(a)], LMO-B delivered the biggest capacity below 4.5 V compared to the other three samples. This might have been due to the fact that the tubular morphology of LMO-B had good contact with the electrolyte and resulted in the efficient oxidation of $Ni^{2+} \rightarrow Ni^{4+}$ and $Co^{3+} \rightarrow Co^{4+}$. After 50 charge/discharge cycles, LMO-B still had the best performance and delivered a value of 199.1 mAh/g, but LMO-C presented a rapid capacity loss, which remained at 114.5 mAh/g. LMO-A and LMO-D presented relatively good cycle performance and delivered values of 161.5 and 162.6 mAh/g at the 50th cycle. Because their morphologies were composed by the ordered aggregation of nanoparticles, the crystal structure of

LMO-A and LMO-D were relatively stable during 50 charge/discharge cycles.

The cycle performance of LMO-B at various current densities is presented in Figure 9 (other samples are not shown here). The batteries are charged/discharged for six cycles at 0.1 C before they were carried out at high current densities. LMO-B presented good cyclic performance at various current densities. For example, LMO-B delivered initial capacities of 245.3, 178.8, 127.5, and 82.3 mAh/g at 0.1, 1, 2, and 5 C rates, respectively. The tubular structure of LMO-B supported the sufficient lithium extraction/reinsertion and rapid lithium diffusion ability; this reflected the improved high-rate performance.

CONCLUSIONS

A series of LMO cathode materials were successfully synthesized with PAN as a template. The concentration of PAN in the starting solution of PAN with DMF played an important role in the fiber morphologies of the PAN/LMOs. Along with the decrease in the concentration of PAN in the precursor, the diameters of the PAN/LMO fibers were decreased. From starting ratios of 1:9 and 1:14 of PAN to DMF, micrometer-long PAN fibers were electrospun, but PAN/DMF ratios of 1:10 and 1:12 resulted in electrospinning millimeter-long fibers of PAN. In the interface of PAN and metal salts, LMOs were grown and were
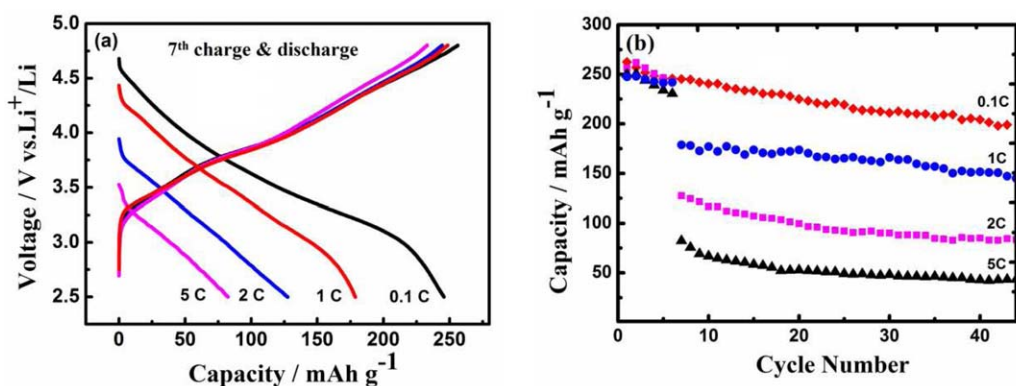

Figure 9. Charge/discharge profiles and cycling performance of LMO-B charged at 0.1 C and discharged at different current rates of 0.1, 1, 2, and 5 C in the voltage range 2.5–4.8 V. [Color figure can be viewed in the online issue, which is available at wileyonlinelibrary.com.]

accompanied by the decomposition of PAN; the crystal morphologies of LMO were quite dependent on the diameter and length of the PAN/LMO fibers. Short fibers of PAN were decomposed, and the organic species were removed through the interspace of PAN/LMO, and LMO crystals grew and aggregated on the morphologies along the template of PAN. The long PAN fibers hindered the removal of small molecules, and the inner pressure resulted in the crystals growing toward the outside of the fibers to form tubular structure of LMO. LMO sample with tubular structure provided good contact with electrolyte and resulted in efficient redox processes; this delivered a good capacity of 262.3 mAh/g at cutoff voltages of 2.5–4.8 V at 0.1 C rate. Benefitting from the unique tubular structure, the sample also exhibited a good rate and cycling performance.

ACKNOWLEDGMENTS

REFERENCES

1. Tarascon, J. M.; Armand, M. *Nature* **2001**, *414*, 359.

2. Song, H.-K.; Lee, K. T.; Kim, M. G.; Nazar, L. F.; Cho, J. *Adv. Funct. Mater.* **2010**, *20*, 3818.

3. Goodenough, J. B.; Park, K. S. *J. Am. Chem. Soc.* **2013**, *135*, 1167.

4. Yamada, A.; Chung, S. C.; Hinokuma, K. *J. Electrochem. Soc. A* **2013**, *148*, 224.

5. Thackeray, M. M.; Kang, S. H.; Johnson, C. S.; Vaughey, J. T.; Benedek, R.; Hackney, S. A.; Fell, C. R.; Lee, D. H.; Meng, Y. S.; Gallardo-Amores, J. M.; Moran, E.; Dompablo, M. E. A. *Energy Environ. Sci.* **2012**, *5*, 6214.

6. Thackeray, M. M.; Kang, S. H.; Johnson, C. S.; Vaughey, J. T.; Benedek, R.; Hackney, S. A. *J. Mater. Chem.* **2007**, *17*, 3112.

7. Ito, A.; Li, D.; Sato, Y.; Arao, M.; Watanabe, M.; Hatano, M.; Horie, H.; Ohsawa, Y. *J. Power Sources* **2010**, *195*, 567.

8. Armstrong, A. R.; Holzapfel, M.; Novak, P.; Johnson, C. S.; Kang, S. H.; Thackeray, M. M.; Bruce, P. G. *J. Am. Chem. Soc.* **2006**, *128*, 8694.

9. Wang, Z.; Liu, E.; He, C.; Shi, C.; Li, J.; Zhao, N. *J. Power Sources* **2013**, *236*, 25.

10. Min, J. W.; Yim, C. J.; Im, W. B. *Appl. Mater. Interfaces* **2013**, *5*, 7765.

11. Miao, X. W.; Ni, H.; Zhang, H.; Wang, C. G.; Fang, J. H.; Yang, G. *J. Power Sources* **2014**, *264*, 147.

12. Jiang, K. C.; Wu, X. L.; Yin, Y. X.; Lee, J. S.; Kim, J.; Guo, Y. G. *ACS Appl. Mater. Interfaces* **2012**, *4*, 4858.

13. Zhao, Y.; Sun, G.; Wu, R. *Electrochim. Acta* **2013**, *96*, 291.

14. Wang, W.; Guo, Y. Y.; Liu, L. X.; Wang, S. X.; Yang, X. J.; Guo, H. *J. Power Sources* **2014**, *245*, 624.

15. Liu, L.; Guo, Y.; Wang, Y.; Yang, X.; Wang, S.; Guo, H. *Electrochim. Acta* **2013**, *114*, 42.

16. Kim, M. G.; Jo, M.; Hong, Y. S.; Cho, J. *Chem. Commun.* **2009**, *2*, 218.

17. Li, L.; Zhang, X. X.; Chen, R. J.; Zhao, T. L.; Lu, J.; Wu, F.; Amin, K. *J. Power Sources* **2014**, *249*, 28.

18. Jin, X.; Xua, Q. J.; Yuan, X. L.; Zhou, L. Z.; Xia, Y. Y. *Electrochim. Acta* **2013**, *114*, 605.

19. Yu, F.; Wu, B. R.; Xu, H. L.; Wu, F. *Adv. Mater. Res.* **2014**, *860*, 928.

20. Li, D.; Xia, Y. N. *Nano Lett.* **2003**, *3*, 555.

21. Yang, G.; Li, Y. H.; Ji, H. M.; Wang, H. Y.; Gao, P.; Wang, L.; Liu, H. D.; Pinto, J.; Jiang, X. F. *J. Power Sources* **2012**, *216*, 353.

22. Mizuno, Y.; Hosono, E.; Saito, T.; Okubo, M.; Nishio-Hamane, D.; Oh-Ishi, K.; Kudo, T.; Zhou, H. S. *J. Phys. Chem. C* **2012**, *116*, 10774.

23. Gu, Y. X.; Chen, D. R.; Jiao, X. L.; Liu, F. F. *J. Mater. Chem.* **2007**, *17*, 1769.

24. Sun, K.; Lu, H. W.; Li, D.; Zeng, W.; Li, Y. S.; Fu, Z. W. *J. Inorg. Mater.* **2009**, *24*, 357.

25. Ding, Y. H.; Zhang, P.; Long, Z. L.; Jiang, Y.; Gao, D. S. *J. Alloys Compd.* **2008**, *462*, 340.

26. Zhu, C. B.; Yu, Y.; Gu, L.; Weichert, K.; Maier, J. *Angew. Chem. Int. Ed.* **2011**, *50*, 6278.

27. Gu, Y. X.; Chen, D. R.; Jiao, M. L. *J. Phys. Chem. B* **2005**, *109*, 17901.

28. Ding, Y. H.; Zhang, P.; Long, Z. L.; Jiang, Y.; Xu, F. *J. Alloys Compd.* **2009**, *487*, 507.

29. Kang, C.-S.; Kim, C.; Kim, J.-E.; Lim, J.-H.; Son, J.-T. *J. Phys. Chem. Solids* **2013**, *74*, 536.

30. Barua, B.; Saha, M. C. *J. Appl. Polym. Sci.* **2015**, *132*, 41918.

31. Xu, G. F.; Li, J. L.; Li, X. P.; Zhou, H. W.; Ding, X. N.; Wang, X. D.; Kang, F. Y. *Electrochim. Acta* **2015**, *173*, 672.

32. Xiang, Y.; Yin, Z.; Zhang, Y.; Li, X. *Electrochim. Acta* **2013**, *91*, 214.

33. Sedghi, A.; Farsani, R. E.; Shokuhfar, A. *J. Mater. Process. Technol.* **2008**, *98*, 60.

34. Rahaman, M. S. A.; Ismail, A. F.; Mustafa, A. *Polym. Degrad. Stab.* **2007**, *92*, 1421.

35. Ji, L. W.; Jung, K. -H.; Medford, A. J.; Zhang, X. W. *J. Mater. Chem.* **2009**, *19*, 4992.

36. Kim, J. S.; Johnson, C. S.; Vaughey, J. T.; Thackeray, M. M.; Hackney, S. A.; Yoon, W.; Grey, C. P. *Chem. Mater.* **2004**, *16*, 1996.

37. Ohzuku, T.; Ueda, A.; Nagayama, M. *J. Electrochem. Soc.* **1993**, *140*, 1862.

38. Wang, H. Y.; Gao, P.; Lu, S. F.; Liu, H. D.; Yang, G.; Pinto, J.; Jiang, X. F. *Electrochim. Acta* **2011**, *58*, 44.

39. Thackeray, M. M.; Johnson, C. S.; Vaughey, J. T.; Li, N.; Hackney, S. A. *J. Mater. Chem.* **2005**, *15*, 2257.

40. Johnson, C. S.; Li, N.; Lefief, C.; Vaughey, J. T.; Thackeray, M. M. *Chem. Mater.* **2008**, *20*, 6095.